



CHORUS

This is the accepted manuscript made available via CHORUS. The article has been published as:

Sound velocity, shear modulus, and shock melting of beryllium along the Hugoniot

Chad A. McCoy, Marcus D. Knudson, and Michael P. Desjarlais

Phys. Rev. B **100**, 054107 — Published 20 August 2019

DOI: [10.1103/PhysRevB.100.054107](https://doi.org/10.1103/PhysRevB.100.054107)

Sound velocity, shear modulus, and shock melting of beryllium along the Hugoniot

Chad A. McCoy*, Marcus D. Knudson, and Michael P. Desjarlais

Sandia National Laboratories, Albuquerque, NM, 87185, USA

**camccoy@sandia.gov*

Magnetically-launched flyer plates were used to investigate the shock response of beryllium between 90 and 300 GPa. Solid aluminum flyer plates drove steady shocks into polycrystalline beryllium to constrain the Hugoniot from 90 to 190 GPa. Multi-layered copper/aluminum flyer plates generated a shock followed by an overtaking rarefaction which was used to determine the sound velocity in both solid and liquid beryllium between 130 and 300 GPa. Disappearance of the longitudinal wave was used to identify the onset of melt along the Hugoniot and measurements were compared to density functional theory calculations to explore the proposed hcp-bcc transition at high pressure. The onset of melt along the Hugoniot was identified at ~205 GPa, which is in good agreement with theoretical predictions. These results show no clear indication of an hcp-bcc transition prior to melt along the beryllium Hugoniot. Rather, the shear stress, determined from the release wave profiles, was found to gradually decrease with stress and eventually vanish at the onset of melt.

I. Introduction:

Among metals, beryllium has one of the highest strength-to-weight ratios and elastic moduli, with an elastic stiffness comparable to steel but at less than a quarter the density.^{1,2} It exists in the hexagonal-close-packed (hcp) structure and has the lowest c/a ratio of any hexagonal metal.³ At ambient conditions, beryllium also has the highest longitudinal sound velocity and lowest Poisson ratio of any metal; consequently it is the only hcp element whose shear modulus exceeds its bulk modulus.³

Currently, beryllium is of particular interest as an ablator or liner material for inertial confinement fusion (ICF)⁴ and magnetized liner inertial fusion (MagLIF)⁵ experiments. In both fusion concepts, beryllium provides a significant advantage over other materials in that it has a higher mass ablation rate,^{6,7} enables better control of hydrodynamic instabilities,^{8,9} and enables the use of lower implosion adiabats.⁴ Recent studies of ICF capsule physics with beryllium ablators¹⁰ found that beryllium capsules exhibit the smallest instability growth rates and can reach the highest theoretical yields of all ablator materials considered.¹¹

Design of ICF and MagLIF experiments require large-scale hydrodynamic simulations to model the implosion and resulting extreme pressure and temperature states. These simulations model the behavior using the conservation relations for mass, momentum, and energy: a set of equations that is closed by inclusion of an equation of state (EOS).¹² Because the EOS of a material depends on its phase, knowledge of the beryllium phase diagram is critical to understanding the behavior of the liner or shell throughout a MagLIF or ICF experiment. In MagLIF experiments, the imploding liner is compressed quasi-isentropically and remains in the solid phase for the bulk of the implosion.⁵ Accurate prediction of solid-solid phase transitions is critical as the liner will see a sudden change in density and sound velocity, which will affect the propagation of compression waves and can lead to shock formation in the liner. Similarly, in ICF experiments, the compression uses a multi-shock laser pulse with the first pulse tailored to melt the Be ablator while keeping the fuel adiabat as low as possible.⁴ This requires knowledge of the melt behavior of beryllium along the Hugoniot to drive complete melting at the lowest possible adiabat thereby maximizing the fuel compressibility. A key concern in both MagLIF and ICF experiments is the control of hydrodynamic instabilities,^{8,9} the growth of which is related to the

sound velocity in the material. Accurate knowledge of these properties enables design of targets and drive pulses that are less susceptible to instability growth.¹³

Theoretical calculations of the beryllium phase diagram predict a transition to a body-centered-cubic (bcc) structure at high pressure and temperature.¹⁴⁻¹⁷ At ambient temperature, the predicted phase diagrams are in reasonable agreement with the hcp-bcc transition occurring between 390¹⁵ and 415¹⁴ GPa. However, at high temperatures, the predicted hcp-bcc-liquid triple-point varies in pressure and temperature from ~95 GPa and ~3500 K¹⁵ to ~180 GPa and ~4300 K¹⁴. This high temperature discrepancy results in the predicted hcp-bcc transition along the principal Hugoniot differing by ~30 GPa. Experimental studies of the Be phase diagram have yet to constrain the high-pressure hcp-bcc transition and melt curve. At low pressure, a transition from α -Be to β -Be was observed prior to melting in early studies^{18, 19} but was not observed in more recent experiments.²⁰⁻²² At high pressure and temperature, Lazicki *et al* measured the phase diagram up to 205 GPa and 4000 K using x-ray diffraction and found no evidence of the hcp-bcc transition.²¹ Furthermore, their measurements failed to provide clear evidence of melting, and only provide a lower bound on the melt curve.²¹

The high-pressure properties of beryllium have been extensively studied under dynamic compression. In solid Be, the principal Hugoniot has been measured up to ~160 GPa using explosively-driven shocks²³⁻²⁵, single-²⁶ and two-stage²⁷ gas guns, and magnetically-accelerated flyer plates²⁸. Above the melt curve, the Be Hugoniot has been measured to ~1800 GPa using nuclear impedance matching^{29, 30} and laser-driven shocks³¹. Beyond the principal Hugoniot, the sound velocity and strength of beryllium have been investigated using both shock and quasi-isentropic loading. Under shock loading, the bulk and longitudinal wave velocities were measured and used to infer the shear stress in Be up to a peak stress of 35 GPa.³² Quasi-

isentropic loading experiments have measured the shear stress using ramp-release experiments to 110 GPa¹ and Rayleigh-Taylor experiments to 50 GPa².

We report measurements of the Hugoniot, sound velocity, and shear stress of beryllium between 90 and 300 GPa from magnetically-accelerated flyer plate experiments performed on the Sandia Z machine.³³ The beryllium Hugoniot was constrained from 90-190 GPa to resolve a discrepancy between models and existing data. Sound velocity measurements from 130-300 GPa probed the proposed hcp-bcc transition and melting along the Hugoniot. Density functional theory (DFT) calculations were used to identify the expected change in response across the hcp-bcc transition and compared to the experimental results. The onset of melting was determined to occur at ~205 GPa and no clear evidence of an hcp-bcc transition was identified.

II. Experimental Methods:

The beryllium Hugoniot and sound velocity were measured in flyer plate experiments performed on the Sandia Z machine, a pulsed-power generator capable of producing currents greater than 20 MA and magnetic fields exceeding 1000 T with a rise time of ~100-1000 ns.³³ These experiments used an asymmetric coaxial load geometry, with a rectangular cathode stalk surrounded by anode plates with anode-cathode (A-K) gaps of 1.4 and 1.0 mm on the north and south sides, respectively.^{34, 35} The anode plates were designed to be flyer plates which would impact the samples. The asymmetric construction produced different magnetic pressures in the A-K gaps, accelerating the flyer plates to different velocities enabling measurement at two distinct stress states on a single shot.

Three dedicated Hugoniot and seven sound velocity experiments were performed to investigate the properties of beryllium near melt on the Hugoniot. The dedicated Hugoniot experiments used 0.9 mm thick solid aluminum flyer plates and the sound velocity experiments

used 0.7/0.15 mm thick composite Al/Cu flyer plates. The composite flyer plates were fabricated by electroplating copper onto an aluminum “blank” and then diamond-turning both sides to the final desired thickness. The density of the high-purity plated copper was found to be >99% full density (8.93 g/cm³). Simulations with the 1D magnetohydrodynamics code LASLO³⁶ show that the ramp compression wave that accelerates the flyer plate compresses any voids in the copper layer and that the resulting layer is at full density upon impact with the target. For both flyer plate types, simulations imply that the plates have a sufficiently thick (>0.2 mm) solid layer at the impact surface to produce a steady shock which propagates through the target.³⁷

The relative thickness of the copper and aluminum layers for the sound velocity flyer plates were determined in two ways: (1) using acoustic microscopy from both sides of the flyer plate and (2) precision measurements of the flyer plate mass and dimensions. Acoustic microscopy maps the internal features of the flyer plate, identifying the depth of the Al/Cu interface from each side as well as interrogating the adhesion of the copper plating to the aluminum blank. Flyer plates for which the copper was found to have delaminated from the aluminum during final machining were rejected. For the dimensional method the density of the copper and the aluminum were taken to be the measured density of the plated copper and the density of 6061-T6 aluminum (2.70 g/cm³), respectively. The uncertainty in the inferred copper thickness using this method was dominated by the uncertainties in the lateral dimensions of the flyer plate (~10 μm) as measured with the measuring microscope, and the measured density uncertainty of the plated copper (contributes ~2 μm to thickness uncertainty). Overall uncertainty in the thickness of the copper layer (using both methods) was determined to be ~3 μm (~2% of the copper thickness).

Beryllium samples for the dedicated Hugoniot experiments were nominally 6.25×10 mm and 1 or 0.75 mm thick polycrystalline material (S200F, Brush Wellman), backed by either lithium fluoride (LiF) or quartz windows. Adjacent samples were quartz windows which enabled observation of the flyer plate and estimation of the impact time at the beryllium sample. The measured beryllium density was 1.85 g/cm^3 . The backing windows were flash-coated with aluminum on the front surface and antireflective (AR) coated for 532 nm on the back surface.

The beryllium samples for the sound velocity experiments (Figure 1) were stepped polycrystalline material (S200F, Brush Wellman), nominally 25 mm tall by 10 mm wide with thicknesses of 0.5, 0.7, 0.9, and 1.1 mm. A 0.1 mm thick layer of copper was electroplated to the impact surface of the beryllium sample to generate an impact stress above the melt stress for the copper impactor. Without this layer the impactor would have remained solid for most of the experiments described in this manuscript. This would have resulted in a complex release structure from the copper impactor, thereby complicating the experimental analysis. The beryllium step heights were measured with a through-the-lens laser autofocus instrument, with $\sim 1 \text{ }\mu\text{m}$ precision. Measurements were made both prior to and after plating. Bowing of the beryllium sample due to residual stress from the plating process resulted in an uncertainty in the copper thickness of $\sim 2 \text{ }\mu\text{m}$.

Quartz or LiF windows, coated similarly to the dedicated Hugoniot targets, were mounted to the back of the beryllium steps using a low-viscosity epoxy (Angstrombond). The different window materials were chosen to accommodate the measurement of wave profiles. Lower stress experiments (below 150 GPa) utilized LiF windows to enable measurement of the beryllium/LiF interface velocity; LiF has been demonstrated to remain transparent under shock compression to $\sim 210 \text{ GPa}$.³⁸ Higher stress experiments (above 155 GPa, at which stress the resulting shock in the

LiF would render it opaque) utilized α -quartz windows. Above ~ 90 - 100 GPa along the Hugoniot α -quartz becomes reflective, and thus a continuous measurement of the shock velocity can be obtained using velocity interferometry. Similar to the dedicated Hugoniot experiments, adjacent samples were quartz windows which enabled observation of the flyer plate and estimation of the impact time at each step of the beryllium sample.

A multipoint velocity interferometer system for any reflector (VISAR)^{39,40} with 32 independent channels was used to measure the flyer velocity and either the Be/LiF interface velocity or the shock velocity in quartz windows, as shown in Figure 1. The VISAR probe was a Nd:YAG laser that is frequency doubled to 532 nm. Single-crystal quartz is mostly transparent to 532 nm light, allowing the VISAR probe to pass through the windows and reflect off the back surface of the flyer plate, tracking its velocity from rest to impact. A sudden change in phase and amplitude signified the flyer plate impact and shock-breakout at the Be/LiF and Be/quartz interface; these features were used to determine the transit time of the shock wave through the beryllium sample. 2π phase ambiguities were resolved by using either two or three different VISAR sensitivities (measured in velocity-per-fringe (VPF)) at each location. VPF settings ranged from 0.506 to 1.926 km/s/fringe. Velocity uncertainty was conservatively estimated at one-tenth of a fringe, resulting in flyer plate and quartz shock velocity uncertainties of $\sim 0.5\%$ and Be/LiF interface velocity uncertainties of $\sim 1\%$.

III. DFT Calculations:

First-principles molecular dynamics (FPMD) calculations were performed using the Vienna Ab-Initio Simulation Package (VASP), a plane-wave density functional theory (DFT) code developed at the Technical University of Vienna.⁴¹⁻⁴³ For the Hugoniot calculations in this work, the beryllium atoms were represented with projector augmented wave (PAW) potentials⁴⁴,

⁴⁵ and exchange and correlation were modeled with the Perdew-Burke-Ernzerhof (PBE) functional.⁴⁶ A total of 250 atoms were included in the supercell, with a plane-wave cutoff energy of 300 eV. Molecular dynamics simulations were performed in the NVT ensemble, with simple velocity scaling as a thermostat, and typically covered on the order of a few to several picoseconds of real time with time steps of 2 fs. For these calculations the Brillouin zone was sampled by a Γ -centered $2 \times 2 \times 2$ Monkhorst-Pack \mathbf{k} -point grid.⁴⁷ Calculations were performed for hcp, bcc, and liquid.

The Rankine-Hugoniot jump conditions,¹² which are derived by considering conservation of mass, momentum, and energy across a steady propagating wave, provide a set of equations relating the initial energy (E), volume (V), and stress (σ) with steady state, post-shock values

$$(E - E_0) = \frac{1}{2}(\sigma - \sigma_0)(V_0 - V) \quad (1)$$

$$(\sigma - \sigma_0) = \rho_0 U_s u_p \quad (2)$$

$$\rho = \frac{\rho_0 U_s}{U_s - u_p} \quad (3)$$

where ρ , U_s , and u_p denote the density, shock velocity, and particle velocity, respectively, and the subscript 0 denotes initial values. The first of these equations, derived from the conservation of energy, provides a prescription for calculation of the Hugoniot. Temperatures and densities are iterated to obtain final states close to satisfying Eq. 1 for the stress range of interest with the final Hugoniot state obtained through interpolation on those values.

Elastic constants were determined by evaluating small strains ($\sim 1\%$ in both compression and tension). In these evaluations, direct entropy calculations for the solid or liquid⁴⁸ were used to choose ΔT such that the strained system remained on an adiabat ($\Delta S = 0$). For the liquid case

simple isotropic, adiabatic strains were evaluated to determine the adiabatic elastic constants. In the solid cases (both bcc and hcp), the strains were applied along strategically chosen directions such that the independent elastic constants were sampled. For the relatively simple cubic bcc system a single strategically chosen strain tensor provided all three independent elastic constants (c_{11} , c_{12} , and c_{44}). The lower symmetry hcp system required a combination of two strains to provide all five independent elastic constants (c_{11} , c_{12} , c_{13} , c_{33} , and c_{44}). Note that the equivalence $c_{66} = (c_{11} - c_{12})/2$ was evaluated and found to be satisfied, lending confidence in the method used. The bulk sound velocity for the hcp, bcc, and liquid were also obtained directly from the elastic constant calculations. In order to compare with the experimental measurements, which utilized polycrystalline material, the longitudinal sound velocities for the hcp and bcc solids were determined using a Voigt-Reuss-Hill average⁴⁹. The Poisson ratio and shear modulus were also determined from these calculations and compared with experimental data. These values are listed in Table I and plotted in Figs. 5, 6 and 8.

IV. Analysis:

A. Hugoniot

The beryllium shock velocity was determined from the measured thicknesses and shock wave transit times for the beryllium samples. Since beryllium is opaque the impact time could not be directly observed. Instead, impact times were interpolated from the observed impact times for the adjacent quartz windows. A correction to the impact time, based on the flyer velocity, was applied to account for measured differences in flight distances (typically $<3 \mu\text{m}$). The beryllium Hugoniot state was determined through impedance matching using the Rankine-Hugoniot relations,¹² which identify the Hugoniot state as the intersection of the beryllium Rayleigh line and the backwards-facing aluminum Hugoniot emanating from the measured flyer

plate velocity.¹² The piecewise linear Hugoniot fit given in ref. 50 was used for the aluminum standard in these experiments. Uncertainty in impact and breakout times were conservatively estimated to be 0.5 ns, producing single-sample uncertainties in shock velocity of ~2-3%. The measured shock velocity was averaged for the two sample thicknesses, resulting in a final uncertainty of ~1-2%. Uncertainty in the inferred particle velocity was determined using a Markov-chain Monte Carlo (MCMC) technique and were found to be of order 1%.

B. Sound Velocity

Sound velocities were inferred using the overtaking rarefaction method and observing the decrease in velocity upon overtake of the leading shock by the release wave from the copper-aluminum interface in the flyer plate.³⁵ This technique is similar to previous experiments observing a decrease in emission of a liquid (bromoform) analyzer,^{32, 51, 52} but is less affected by noise and small variations in stress.³⁵ For quartz windowed samples, the reflective shock was tracked using the VISAR diagnostic and the decrease in velocity at overtake was directly observed. A similar technique was used for the LiF windowed samples, however in those cases the Be-LiF interface velocity was tracked rather than the leading shock velocity.

For experiments at peak stresses below melt on the Hugoniot, a complex structure was identified upon release caused by the splitting of the release wave into the longitudinal and bulk waves (Figure 2a). The Be-LiF interface velocity (solid blue line) exhibits a velocity plateau upon the shock entering the LiF followed by a two-stage release. Linear fits were made to the constant-velocity plateau (dotted black line), longitudinal release (dashed yellow line), and bulk release (dashed-dotted red line) regions. The overtake time for the longitudinal wave (yellow star) and bulk wave (red star) was found from the intersection of the release fits with the fit to the plateau region. The uncertainty in intersection time was calculated using a Monte Carlo

technique with 10^6 iterations, where the plateau and overtake fits were recalculated using variable time durations for the fit region. Uncertainties in the overtake times determined in this manner were typically <1 ns.

The beryllium step thicknesses were chosen such that the overtake would occur within the sample for the thicker steps and within the windows for the thinner steps. In cases where the overtake occurred within the sample (i.e. there was no constant-velocity plateau in the VISAR trace), the average of the plateau regions from the thinner steps was used and an effective negative overtake time was determined. The overtake times and step thicknesses were correlated for each of the samples and linearly fit to determine the thickness, d_o , and time, t_o , where overtake would occur in an infinitely thick sample (i.e. in the absence of wave interactions). As seen in Figure 2b, the thicknesses where the longitudinal (dashed yellow line) and bulk (dashed-dotted red line) would overtake the shock at breakout are identified as the overtake thicknesses.

The copper layer on the impact surface of the beryllium sample served to generate a simple release from the Cu/Al interface within the flyer plate (the copper melted upon impact). However, it also complicated somewhat the sound velocity determination from the overtake measurement due to wave interactions at the Cu/Be interface. Upon the shock reaching the Cu/Be interface in the target, a release wave was launched back into the copper. Thus, the overtaking rarefaction from the Cu/Al interface propagated through both shocked copper and partially released copper as seen in Figure 3. The lower density and temperature of the partially released copper decreased the sound velocity relative to the shocked copper, resulting in the rarefaction wave arriving at the Cu/Be interface later than it would have had the partial release not been present.

To account for this wave interaction a scale factor, $S_{C_{l,C}} = \frac{C_{l,C}^{rel}}{C_{l,C}}$, was used to relate the Lagrangian sound velocity of the partially released copper, $C_{l,C}^{rel}$, to that of the shocked copper, $C_{l,C}$. McCoy, Knudson, and Root³⁵ determined that the scale factor for copper releasing into quartz is nominally independent of stress, with a value of $\sim 0.85 \pm 0.11$. We note that a computationally determined scale factor using the SESAME 3325³⁶ EOS table also exhibits a stress independent scale factor of ~ 0.84 , in very good agreement with the experimentally determined value ($\sim 1\%$ lower). In the absence of an experimentally determined scale factor for copper releasing into beryllium, we used a value of 0.81, corresponding to a 1% increase in the scale factor of 0.80 determined computationally from SESAME 3325. The scale factor uncertainty was assumed to be the same as the experimental value from ref. 35, i.e.

$$S_{C_{l,C}} = 0.81 \pm 0.11.$$

The copper Hugoniot and sound velocity were used to determine the times at which the rarefaction, t_R , enters the beryllium sample. The beryllium Lagrangian sound velocity, $C_{l,B}$, was then determined from

$$C_{l,B} = \frac{d_o}{t_o - t_R}. \quad (4)$$

The uncertainty in sound velocity was found to be $\sim 2\text{-}3\%$ and was dominated by the thickness measurements and inferred overtake times. The impact and Be/window breakout times were directly observed with VISAR and resulted in smaller contributions to the overall uncertainty.

C. Shear Stress

The shear stress was estimated using the self-consistent method proposed by Asay and Lipkin.⁵³ This technique assumes the *in-situ* particle velocity is known at multiple points within

the material of interest, and the Lagrangian sound velocity is determined as a function of the particle velocity, as shown in Figure 4. Determination of the *in-situ* particle velocity requires knowledge of the EOS of the window material as well as the interface particle velocity. For the LiF windowed samples (Figure 2a) the interface particle velocity is directly observed with VISAR. For the quartz windowed samples, the VISAR observed the quartz shock velocity rather than the interface particle velocity. To extract the interface velocity, the Lagrangian technique developed by McCoy and Knudson⁵⁴ was used. This correction used the quartz Hugoniot and release model described by Knudson and Desjarlais⁵⁰ with the most recent model calibration coefficients.⁵⁵

Because the shock impedances of quartz and LiF are similar to that of beryllium, the *in-situ* particle velocity for the beryllium samples could be determined accurately through impedance matching. At each time along the wave profile, an impedance match was made between the beryllium and window material in a manner similar to that described in ref. 56. By repeating this for the entire wave profile, the *in-situ* particle velocity was determined as a function of time (solid blue line in Fig. 4). After determining the *in-situ* response, and assuming uniaxial strain, the derivatives of the longitudinal stress (σ) and strain (ϵ), are determined through

$$d\sigma(\epsilon) = d\sigma_m(\epsilon) + \frac{4}{3}d\tau(\epsilon) \text{ and} \quad (5)$$

$$d\epsilon = \frac{du}{C_l(u)}, \quad (6)$$

where σ_m is the mean stress and τ is the shear stress. By substituting the bulk (C_b) and longitudinal (C_l) sound velocities, Eq. 5 can be rewritten as

$$d\tau(\varepsilon) = \frac{3}{4} \rho_0 [C_l^2(\varepsilon) - C_b^2(\varepsilon)] d\varepsilon, \quad (7)$$

where ρ_0 is the initial density. The shear strength can be estimated as $Y = 2\tau$ using the J2 theory¹, which, by substituting Eq. 6 and integrating Eq. 7, gives

$$Y = -\frac{3}{4} \int \frac{C_l^2 - C_b^2}{C_l} du. \quad (8)$$

For each sample the wave profiles for the two thinnest Be steps, where both the longitudinal and bulk release occurred within the window, could be analyzed using Eq. 8 to estimate the shear strength. This provided two independent measurements of the shear stress, which were then averaged to determine a shear stress and uncertainty. Additional details on the calculation can be found in refs. 1 and 53.

V. Results and Discussion:

A. Hugoniot

A total of three dedicated Hugoniot experiments were performed on beryllium, yielding six Hugoniot measurements. The pertinent parameters for these experiments are listed in Table II. v_f and U_s denote the measured flyer plate velocity and the shock velocity in the beryllium, respectively. u_p , σ , and ρ denote the inferred particle velocity, stress, and density of the beryllium in the shocked state, respectively. The Hugoniot is plotted in Fig. 5. Also shown in the figure are data from gas gun measurements conducted by Isbell *et al*²⁷ (green circles) and Wise *et al* (open circles)²⁶, and explosively-driven data from the Marsh compendium (yellow triangles)²³ and Walsh *et al* (open triangles)²⁴. The present results (red diamonds) are significantly less compressible than the Isbell results and agree well with an extrapolation of the other data.

In comparison to EOS models, we find that the present results agree with both tabular models shown: SESAME⁵⁷ 2024 (dashed-dotted black line) and XEOS 40⁵⁸ (dashed blue line; a

QEOS model with similar behavior to the recent multiphase model developed by Benedict et al¹⁴). Density functional theory (DFT) Hugoniot fits were determined for hcp Be ($U_s = 7.766 + 1.182u_p$, solid red line), bcc Be ($U_s = 7.488 + 1.208u_p$, dashed orange line), and liquid Be ($U_s = 7.800 + 1.187u_p$). The experimental data are in excellent agreement with the hcp fit, whereas the bcc fit is systematically more compressible than the data, particularly at the lower stresses. However, we note that over the stress range explored here, the solid and liquid fits cannot be distinguished experimentally. No experimental data exists in the 200-300 GPa stress range, within the liquid phase, to compare with the DFT calculations. We note that inclusion of the copper layer on the impact surface of the sound velocity targets in this study resulted in an inability to measure the Be Hugoniot directly in those experiments. However, due to the agreement between DFT and both the experimental results and tabular models in the solid regime, we chose to use the DFT solid and liquid Hugoniots to calculate the stress, density, and particle velocity of the shocked beryllium for the sound velocity experiments. This differentiated between the solid and liquid phases in Be, and represented the change in Hugoniot slope upon melting absent from the single-phase SESAME and XEOS models.

B. Sound Velocity

Seven sound velocity experiments were conducted, yielding fourteen measurements of the beryllium sound velocity at stresses between 130 and 300 GPa, as shown in Figure 6. Eight of these measurements exhibited a two-wave release structure, as illustrated in Figure 2a, indicative of release from the solid phase. The remaining six measurements exhibited a single-wave release structure, indicative of release from the partially molten or liquid phase. The pertinent parameters for these experiments are listed in Table III. v_f and U_s denote the measured flyer plate and shock velocity, respectively. u_p and σ denote the inferred particle

velocity and peak stress obtained from the DFT Hugoniot for Be and the measured shock velocity. C_l , C_b , G , Y , and ν denote the inferred longitudinal and bulk sound velocities, the shear modulus, the shear strength, and Poisson's ratio, respectively, obtained from the measured overtake times.

The sound velocities and Poisson ratio are plotted in Fig. 6. The peak longitudinal sound velocity (open diamonds) was observed at ~ 150 GPa. At higher stresses, the longitudinal wave velocity begins to decrease rapidly and approaches the bulk sound velocity (red diamonds) near ~ 200 GPa. In contrast, the bulk sound velocity increases monotonically over this stress range.

The Poisson ratio, defined as $\nu = \frac{3C_b^2 - C_l^2}{3C_b^2 + C_l^2}$, was used to determine the onset of melt (Figure 6c); a piecewise linear fit (solid black line) to these data (diamonds), the data of Chhabildas *et al*³² (squares), and the ambient Poisson ratio (yellow triangle)³, suggests an onset of melt at a stress of $\sigma = 204 \pm 13$ GPa.

Using the DFT Hugoniot and ambient thermal Grüneisen parameter, $\Gamma_0 = 1.30$, from Zhang *et al*⁵⁹, the bulk sound velocity was calculated from

$$C_b = V \sqrt{\left(1 - \frac{\Gamma \epsilon V_0}{2V}\right) \left(-\frac{d\sigma}{dV}\bigg|_H\right) + \frac{\rho \Gamma \sigma_H}{2}}, \quad (9)$$

where $V = \frac{1}{\rho}$ is the specific volume and the subscript H denotes the stress and derivative of the stress along the principal Hugoniot.⁶⁰ Here we make the common assumption of $\rho \Gamma$ being constant; i.e., $\Gamma = \frac{\rho_0 \Gamma_0}{\rho}$ in Eq. 9. Under this assumption, the calculated bulk velocity (solid red line) falls within the uncertainty of the measurements reported here as well as those of Chhabildas *et al*³². The discrepancy between these data and the DFT calculations arises from the

Grüneisen parameter; assuming $\rho\Gamma$ to be constant yields $\Gamma \approx 0.75$ at melt on the Hugoniot whereas the DFT calculations imply $\Gamma \approx 0.91$. Previous DFT calculations by Luo¹⁶ with the DFT Γ . While the calculation assuming $\rho\Gamma = \text{constant}$ better matches the data, we don't believe that it accurately represents the Be Grüneisen parameter at these stresses due to the extreme extrapolation from ambient measurement.

The longitudinal sound velocity, calculated using the bulk sound velocity and the fit to the experimentally determined Poisson ratio, is shown as the black dashed line. We note that the bulk sound velocity from the model by Ignatova *et al*⁶¹ (dashed-dotted purple line) agrees with the present results. However, the longitudinal wave velocity from Ignatova (dashed-dotted green line) significantly overpredicts the peak wave velocity compared to this work. This large discrepancy in the longitudinal velocity implies that the Ignatova model does not produce a reasonable value for the high-stress shear modulus of beryllium.

At increasing stress and temperature along the Hugoniot, beryllium is predicted to undergo a solid-solid phase transition from the hexagonal-close-packed to body-centered-cubic (hcp-bcc) phase at a stress just below the melt boundary. Different calculations of the phase diagram (see Fig. 7) predict the hcp-bcc transition along the Hugoniot in the stress range from ~ 165 ¹⁵ and ~ 195 ¹⁴ GPa, and melt along the Hugoniot between ~ 205 and ~ 210 GPa. These predictions for melt along the Hugoniot appear to be in good agreement with the present experimental results, as illustrated by the Poisson ratio shown in Figure 6c.

DFT calculations for solid Be (see Fig. 6b) show essentially no difference between the bulk velocity (solid symbols) in the hcp (triangles) and bcc (circles) phases. A small difference (~ 0.3 km/s) is seen between the hcp and bcc longitudinal velocities (open symbols), with the hcp phase exhibiting a consistently higher value. Given the relative size of the experimental

uncertainty and the predicted difference in longitudinal velocity for the two phases, the present results are incapable of resolving between the two. In particular, the observed steady decrease in longitudinal velocity between ~ 150 - 200 GPa is consistent with either a steady decrease in the shear modulus and loss of strength as melt is approached or an hcp-bcc transition.

This lack of conclusive evidence for a solid-solid phase transition is in agreement with the laser-heated diamond anvil cell work by Lazicki *et al.*²¹ In that study diffraction measurements only observed the hcp phase for P-T conditions up to 195 GPa and 4000 K. These conditions are well into the bcc regions defined by Robert¹⁵ and Luo¹⁶, but potentially fall short of the transition boundaries predicted by Benedict¹⁴ and Xian¹⁷. However, as noted by Robert, the predicted location of the hcp-bcc boundary has large uncertainty due to the small enthalpy difference between the two phases. Conclusive evidence for the bcc phase would require phase-sensitive measurements, such as diffraction. Further investigation of the hcp-bcc phase boundary in this region would require use of shock-ramp compression techniques to reach the transition stress while remaining at temperatures below the melt curve.

At stresses above the onset of melt along the Hugoniot, only the bulk sound velocity (yellow diamonds) is observed. In this stress regime the experimental data are in excellent agreement with the DFT calculations (dashes). In ICF experiments, the first shock is tailored to melt the ablator, with the subsequent shocks driving the implosion of the capsule.⁶² As growth rates and oscillation periods of the ablative Richtmyer-Meshkov instability are sensitive to the sound velocity in the shocked fluid⁶³, use of the DFT liquid sound velocity would be recommended for hydrodynamic simulations of ICF capsules with Be ablaters.

a. Shear Modulus

The shear modulus, G , can be estimated from the longitudinal and bulk wave velocities of shocked beryllium through the relation

$$G = \frac{3}{4} \rho (C_l^2 - C_b^2). \quad (10)$$

As shown in Figure 8, the peak shear modulus inferred from this study (red diamonds) is ~ 240 GPa. This is in good agreement with the peak values measured by Chhabildas et al (black squares)³² for shock compression up to 34 GPa. Using the calculated bulk velocity and the piecewise linear fit to the Poisson ratio shown in Fig. 6c, a model for the shear modulus can be constructed (solid red line). This model for the shear modulus, which exhibits a maximum of ~ 260 GPa at a stress of ~ 90 GPa on the Hugoniot, is in good agreement with the values inferred from the present study and Chhabildas et al.

The only other experimentally inferred values for the shear modulus are from Brown et al. (yellow triangles), obtained from quasi-isentropic (ramp) compression experiments. The values reported by Brown et al are in good agreement with those of Chhabildas et al and our experimentally derived model for stresses below 50 GPa. At stresses of ~ 80 -100 GPa the values reported by Brown et al are somewhat higher than our model. We note that the values reported by Brown et al are from quasi-isentropic compression experiments, and at these stresses the shock temperature exceeds that of the isentrope by ~ 1000 K. This difference might be sufficient to explain the shear modulus discrepancy between our model and the values reported by Brown et al.

Also shown in Fig.8 are calculations of the shear modulus using various strength and EOS models for Be. Calculations were performed using the Steinberg-Guinan strength model (short-dashed blue line) and the SESAME 2024 table with the elastic constants from ref. 64, and the Burakovsky-Preston strength model (long-dashed blue line) with the Simon fit presented in

Eq. 28 of ref. 65. Temperature dependence of the shear modulus was modeled using a fit to the average values from Nadal and Bourgeois⁶⁶ and extrapolated linearly to higher temperature. Calculations were also performed using both the Steinberg-Guinan and Burakovsky-Preston strength models with the XEOS 40 table shown in Figure 5. This calculation gave approximately the same values as SESAME 2024, so only the one table is shown for clarity. The Burakovsky-Preston model is in better agreement with the data and experimental fits than the Steinberg-Guinan model. This is expected as the Burakovsky-Preston model updated the Steinberg-Guinan model to correct the insufficient negative curvature which resulted in overprediction of the shear modulus at moderate compression. The RING model (dashed-dotted purple line)⁶¹ overpredicts the Be shear modulus along the Hugoniot for the entire stress range up to shock-melting. We note that at ambient conditions, the RING model predicts a shear modulus ~25% greater than experiment. Decreasing the model by this amount would reduce the peak value by more than 100 GPa and bring the calculation into better agreement with the other models and experimental data.

C. Shear Stress

The inferred shear stress from these experiments, shown in Fig. 9, constrains the strength of beryllium for stresses above 100 GPa and temperatures approaching the melt curve. Data from this work (red diamonds) exhibit a steady decrease in strength along the Hugoniot, culminating with complete strength loss upon melting at a stress of just over 200 GPa. The peak shear strength inferred in this work was ~3.5 GPa, which is in good agreement with the peak shear strength inferred by Brown (yellow triangles)¹ and Bat'kov (open circles)⁶⁷. At stresses below 50 GPa, both the Brown and Bat'kov results agree with those of Chhabildas (black squares)³², such that the yield curve of solid beryllium can be constrained for all stresses accessible under single-shock compression.

The Steinberg-Guinan (dashed blue line)⁶⁴ strength model for beryllium agrees with the experimental results up to the peak shear stress. However, conventional models fail to accurately capture the loss of strength exhibited experimentally as the melt stress is approached. To account for this, the RING relaxation model (dashed-dotted purple line)⁶¹ and earlier phenomenological model of strength (PMS, solid black line)⁶⁸ developed by VNIIEF scale the shear stress by a factor of $1 - \frac{T}{T_m}$, where T_m is the melt temperature at a given stress. This construct is similar to the Preston-Tonks-Wallace (PTW)⁶⁹ temperature correction factor of $1 - \alpha \frac{T}{T_m}$; the coefficient α prevents the PTW model from vanishing at melt and is not present in the VNIIEF models. Both VNIIEF models adequately represent the experimental data up to 100 GPa. However, the RING model systematically under predicts the shear stress as melt is approached. In contrast, the PMS model remains in good agreement with the experimental data. This conclusion contradicts the work of Henry de Frahan, *et al*². They found that the RING model best represented the experimental results at low stresses. This indicates that while a relaxation model, such as RING, may accurately represent the behavior at low stresses, the accuracy may decrease for stress and temperature conditions approaching melt.

VI. Conclusions

The principal Hugoniot, sound velocity and shear stress of beryllium were measured using magnetically-accelerated flyer plates on the Sandia Z machine. Hugoniot measurements further constrained the solid behavior from 90-190 GPa and were in good agreement with lower-stress data and DFT calculations. However, these results and DFT calculations do not agree with results reported by Isbell *et al*²⁷ for solid Be above 90 GPa. The agreement between these results

and the DFT calculations for the hcp phase lend confidence for the use of DFT for liquid Be where experimental data is sparse.

The bulk and longitudinal sound velocity were measured over the stress range of 130-300 GPa to investigate the melt behavior of Be. In the solid phase, the bulk sound velocity is slightly higher than predictions from DFT calculations for both the bcc and hcp phases but is in good agreement with a Mie-Grüneisen calculation using the DFT Hugoniot and ambient data. Measurements above the melt transition are in good agreement with DFT calculations for the liquid phase. The longitudinal sound velocity is in better agreement with calculations for the hcp phase below 150 GPa; this also agrees with calculated phase diagrams which predict the hcp-bcc transition at stresses above 165 GPa. Above 150 GPa, the longitudinal velocity decreases monotonically until the onset of melt at ~205 GPa. No clear evidence for the hcp-bcc transition was identified from the sound velocity measurements.

The shear modulus and shear stress were determined for solid beryllium approaching melt. The peak value of the shear modulus is in reasonable agreement with the Burakovsky-Preston strength model but occurs at a peak stress ~50 GPa lower than predicted by that model. The present results are within the uncertainty of previous data when adjusted for temperature differences between the Hugoniot and isentrope. Measurements of the shear stress are in good agreement with earlier data and the PMS and RING models developed by VNIIEF. This work suggests that ~50 GPa prior to melt, Be begins to exhibit a gradual loss of strength that continues until the onset of melt.

These results and DFT calculations suggest that the phase diagram of Benedict *et al*¹⁴ best represents the high pressure and temperature response of beryllium and the expected hcp-bcc transition. Furthermore, use of the DFT Hugoniot and liquid sound velocity presented here

will allow for more robust ICF and MagLIF designs, increasing the likelihood of successful experimental designs.

VII. Acknowledgements

Sandia National Laboratories is a multimission laboratory managed and operated by National Technology & Engineering Solutions of Sandia, LLC, a wholly owned subsidiary of Honeywell International Inc., for the U.S. Department of Energy's National Nuclear Security Administration under contract DE-NA0003525. This paper describes objective technical results and analysis. Any subjective views or opinions that might be expressed in the paper do not necessarily represent the views of the U.S. Department of Energy or the United States Government.

1. J. L. Brown, M. D. Knudson, C. S. Alexander and J. R. Asay, *J. Appl. Phys.* **116**, 033502 (2014).
2. M. T. Henry de Frahan, J. L. Belof, R. M. Cavallo, V. A. Raevsky, O. N. Ignatova, A. Lebedev, D. S. Ancheta, B. S. El-dasher, J. N. Florando, G. F. Gallegos, E. Johnsen and M. M. LeBlanc, *J. Appl. Phys.* **117**, 225901 (2015).
3. A. Migliori, H. Ledbetter, D. J. Thoma and T. W. Darling, *J. Appl. Phys.* **95**, 2436-2440 (2004).
4. A. N. Simakov, D. C. Wilson, S. A. Yi, J. L. Kline, D. S. Clark, J. L. Milovich, J. D. Salmonson and S. H. Batha, *Phys. Plasmas* **21**, 022701 (2014).
5. R. D. McBride, M. R. Martin, R. W. Lemke, J. B. Greenly, C. A. Jennings, D. C. Rovang, D. B. Sinars, M. E. Cuneo, M. C. Herrmann, S. A. Slutz, C. W. Nakhleh, D. D. Ryutov, J.-P. Davis, D. G. Flicker, B. E. Blue, K. Tomlinson, D. Schroen, R. M. Stamm, G. E. Smith, J. K. Moore, T. J. Rogers, G. K. Robertson, R. J. Kamm, I. C. Smith, M. Savage, W. A. Stygar, G. A. Rochau, M. Jones, M. R. Lopez, J. L. Porter and M. K. Matzen, *Phys. Plasmas* **20**, 056309 (2013).
6. R. E. Olson, R. J. Leeper, A. Nobile, J. A. Oertel, G. A. Chandler, K. Cochrane, S. C. Dropinski, S. Evans, S. W. Haan, J. L. Kaae, J. P. Knauer, K. Lash, L. P. Mix, A. Nikroo, G. A. Rochau, G. Rivera, C. Russell, D. Schroen, R. J. Sebring, D. L. Tanner, R. E. Turner and R. J. Wallace, *Phys. Plasmas* **11**, 2778-2789 (2004).
7. R. E. Olson, G. A. Rochau, O. L. Landen and R. J. Leeper, *Phys. Plasmas* **18**, 032706 (2011).

8. S. A. Yi, A. N. Simakov, D. C. Wilson, R. E. Olson, J. L. Kline, D. S. Clark, B. A. Hammel, J. L. Milovich, J. D. Salmonson, B. J. Koziolowski and S. H. Batha, *Phys. Plasmas* **21**, 092701 (2014).
9. E. N. Loomis, S. R. Greenfield, R. P. Johnson, J. A. Cobble, S. N. Luo, D. S. Montgomery and M. M. Marinak, *Phys. Plasmas* **17**, 056308 (2010).
10. J. L. Kline, S. A. Yi, A. N. Simakov, R. E. Olson, D. C. Wilson, G. A. Kyrala, T. S. Perry, S. H. Batha, A. B. Zylstra, E. L. Dewald, R. Tommasini, J. E. Ralph, D. J. Strozzi, A. G. MacPhee, D. A. Callahan, D. E. Hinkel, O. A. Hurricane, J. L. Milovich, J. R. Rygg, S. F. Khan, S. W. Haan, P. M. Celliers, D. S. Clark, B. A. Hammel, B. Koziolowski, M. B. Schneider, M. Marinak, H. G. Rinderknecht, H. F. Robey, J. D. Salmonson, P. K. Patel, T. Ma, M. J. Edwards, M. Stadermann, S. Baxamusa, C. Alford, M. Wang, A. Nikroo, N. Rice, D. Hoover, K. P. Youngblood, H. Xu, H. Huang and H. Sio, *Phys. Plasmas* **23**, 056310 (2016).
11. D. S. Clark, A. L. Kritcher, S. A. Yi, A. B. Zylstra, S. W. Haan and C. R. Weber, *Phys. Plasmas* **25**, 032703 (2018).
12. Y. B. Zel'dovich and Y. P. Raizer, *Physics of Shock Waves and High-Temperature Hydrodynamic Phenomena*. (Dover Publications, 2002).
13. J. L. Peterson, D. S. Clark, L. P. Masse and L. J. Suter, *Phys. Plasmas* **21**, 092710 (2014).
14. L. X. Benedict, T. Ogitsu, A. Trave, C. J. Wu, P. A. Sterne and E. Schwegler, *Phys. Rev. B* **79**, 064106 (2009).
15. G. Robert, P. Legrand and S. Bernard, *Phys. Rev. B* **82**, 104118 (2010).
16. F. Luo, L.-C. Cai, X.-R. Chen, F.-Q. Jing and D. Alfè, *J. Appl. Phys.* **111**, 053503 (2012).
17. J.-W. Xian, J. Yan, H.-F. Liu, T. Sun, G.-M. Zhang, X.-Y. Gao and H.-F. Song, *Phys. Rev. B* **99**, 064102 (2019).

18. A. J. Martin and A. Moore, *Journal of the Less Common Metals* **1**, 85-93 (1959).
19. L. C. Ming and M. H. Manghnani, *J. Phys. F: Metal Physics* **14**, L1-L8 (1984).
20. W. J. Evans, M. J. Lipp, H. Cynn, C. S. Yoo, M. Somayazulu, D. Häusermann, G. Shen and V. Prakapenka, *Phys. Rev. B* **72**, 094113 (2005).
21. A. Lazicki, A. Dewaele, P. Loubeyre and M. Mezouar, *Phys. Rev. B* **86**, 174118 (2012).
22. K. Nakano, Y. Akahama and H. Kawamura, *J. Phys.: Condensed Matter* **14**, 10569-10573 (2002).
23. S. P. Marsh, *LASL Shock Hugoniot Data*. (University of California Press, Berkeley, CA, 1980).
24. J. M. Walsh, M. H. Rice, R. G. McQueen and F. L. Yarger, *Phys. Rev.* **108**, 196-216 (1957).
25. R. G. McQueen, S. P. Marsh, J. W. Taylor, J. N. Fritz and W. J. Carter, in *High-Velocity Impact Phenomena*, edited by R. Kinslow (Academic Press, New York, 1970), pp. 293–417.
26. J. L. Wise, L. C. Chhabildas and J. R. Asay, *AIP Conf. Proc.* **78**, 417-421 (1982).
27. W. M. Isbell, F. H. Shipman and A. H. Jones, General Motors Corp., Material Science Laboratory Report MSL-68-13, 1968.
28. D. Swift, D. Paisley and M. Knudson, *AIP Conf. Proc.* **706**, 119-122 (2004).
29. W. J. Nellis, A. C. Mitchell and D. A. Young, *J. Appl. Phys.* **93**, 304-310 (2003).
30. C. E. Ragan III, *Phys. Rev. A* **25**, 3360–3375 (1982).
31. R. Cauble, T. S. Perry, D. R. Bach, K. S. Budil, B. A. Hammel, G. W. Collins, D. M. Gold, J. Dunn, P. Celliers, L. B. Da Silva, M. E. Foord, R. J. Wallace, R. E. Stewart and N. C. Woolsey, *Phys. Rev. Lett.* **80**, 1248–1251 (1998).
32. L. C. Chhabildas, J. L. Wise and J. R. Asay, *AIP Conf. Proc.* **78**, 422-426 (1982).

33. M. E. Savage, L. F. Bennett, D. E. Bliss, W. T. Clark, R. S. Coats, J. M. Elizondo, K. R. LeChien, H. C. Harjes, J. M. Lehr, J. E. Maenchen, D. H. McDaniel, M. F. Pasik, T. D. Pointon, A. C. Owen, D. B. Seidel, D. L. Smith, B. S. Stoltzfus, K. W. Struve, W. A. Stygar, L. K. Warne, J. R. Woodworth, C. W. Mendel, K. R. Prestwich, R. W. Shoup, D. L. Johnson, J. P. Corley, K. C. Hodge, T. C. Wagoner and P. E. Wakeland, in *Proceedings of the 16th IEEE Pulsed Power and Plasma Science Conference, Albuquerque, NM*, edited by E. Schamiloglu and F. Peterkin (IEEE, Piscataway, NJ, 2007), p. 979..
34. M. D. Knudson, R. Lemke, D. Hayes, C. A. Hall, C. Deeney and J. Asay, *J. Appl. Phys.* **94**, 4420-4431 (2003).
35. C. A. McCoy, M. D. Knudson and S. Root, *Phys. Rev. B* **96**, 174109 (2017).
36. J. H. Carpenter, *Private Communication* (2016).
37. R. W. Lemke, M. D. Knudson, D. E. Bliss, K. Cochrane, J.-P. Davis, A. A. Giunta, H. C. Harjes and S. A. Slutz, *J. Appl. Phys.* **98**, 073530 (2005).
38. P. Rigg, M. Knudson, R. Scharff and R. Hixson, *J. Appl. Phys.* **116**, 033515 (2014).
39. L. M. Barker and R. E. Hollenbach, *J. Appl. Phys.* **43**, 4669–4675 (1972).
40. L. M. Barker and K. W. Schuler, *J. Appl. Phys.* **45**, 3692–3693 (1974).
41. G. Kresse and J. Hafner, *Phys. Rev. B* **47**, 558-561 (1993).
42. G. Kresse and J. Hafner, *Phys. Rev. B* **49**, 14251-14269 (1994).
43. G. Kresse and J. Furthmüller, *Phys. Rev. B* **54**, 11169-11186 (1996).
44. P. E. Blöchl, *Phys. Rev. B* **50**, 17953-17979 (1994).
45. G. Kresse and D. Joubert, *Phys. Rev. B* **59**, 1758-1775 (1999).
46. J. P. Perdew, K. Burke and M. Ernzerhof, *Phys. Rev. Lett.* **77**, 3865-3868 (1996).
47. H. J. Monkhorst and J. D. Pack, *Phys. Rev. B* **13**, 5188-5192 (1976).

48. M. P. Desjarlais, Phys. Rev. E **88**, 062145 (2013).
49. R. Hill, Proc. Phys. Soc. London, Sec. A **65**, 349-354 (1952).
50. M. D. Knudson and M. P. Desjarlais, Phys. Rev. B **88**, 184107 (2013).
51. L. V. Al'Tshuler, S. B. Kormer, M. I. Brazhnik, L. A. Vladimirov, M. P. Speranskaya and A. I. Funtikov, Sov. Phys. JETP **11**, 766 (1960).
52. J. H. Nguyen, M. C. Akin, R. Chau, D. E. Fratanduono, W. P. Ambrose, O. V. Fat'yanov, P. D. Asimow and N. C. Holmes, Phys. Rev. B **89**, 174109 (2014).
53. J. R. Asay and J. Lipkin, J. Appl. Phys. **49**, 4242-4247 (1978).
54. C. A. McCoy and M. D. Knudson, J. Appl. Phys. **122**, 085901 (2017).
55. M. P. Desjarlais, M. D. Knudson and K. R. Cochrane, J. Appl. Phys. **122**, 035903 (2017).
56. J. Lipkin and J. R. Asay, J. Appl. Phys. **48**, 182-189 (1977).
57. S. P. Lyon and J. D. Johnson, Report No. LA-UR-92-3407, 1992.
58. P. A. Sterne, L. X. Benedict, S. Hamel, A. A. Correa, J. L. Milovich, M. M. Marinak, P. M. Celliers and D. E. Fratanduono, J. Phys.: Conf. Ser. **717**, 012082 (2016).
59. J. Zhang, J. Zhu, N. Velisavljevic, L. Wang and Y. Zhao, J. Appl. Phys. **114**, 173509 (2013).
60. D. Hayes, R. S. Hixson and R. G. McQueen, AIP Conf. Proc. **505**, 483-488 (2000).
61. O. N. Ignatova, V. A. Raevsky and S. S. Nadezin, AIP Conf. Proc. **1426**, 1145-1148 (2012).
62. B. A. Hammel and the National Ignition Campaign Team, Plasma Phys. Control. Fusion **48**, B497 (2006).

63. V. N. Goncharov, O. V. Gotchev, E. Vianello, T. R. Boehly, J. P. Knauer, P. W. McKenty, P. B. Radha, S. P. Regan, T. C. Sangster and S. Skupsky, *Phys. Plasmas* **13**, 012702 (2006).
64. D. J. Steinberg, S. G. Cochran and M. W. Guinan, *J. Appl. Phys.* **51**, 1498-1504 (1980).
65. L. Burakovsky and D. L. Preston, *J. Phys. Chem. Solids* **67**, 1930-1936 (2006).
66. M.-H. Nadal and L. Bourgeois, *J. Appl. Phys.* **108**, 033512 (2010).
67. Y. V. Bat'kov, A. P. Bolshakov, G. B. L., S. A. Novikov and V. A. Sinitsyn, *Deformation and strength characteristics of beryllium at high loading rates*. (Review, Moscow, 1990).
68. V. V. Igonin, *Berllium Dynamic Strength Measurements: Report on Task 1 Agreement #B590737*. (Lawrence Livermore National Laboratory, 2014).
69. D. L. Preston, D. L. Tonks and D. C. Wallace, *J. Appl. Phys.* **93**, 211-220 (2003).

Table I: DFT calculations of the sound velocity in solid and liquid Be. P , ρ , U_s , u_p , T , C_b , C_l , G , and ν are the pressure, density, shock velocity, particle velocity, temperature, bulk sound velocity, longitudinal sound velocity, shear modulus, and Poisson ratio, respectively. In the liquid phase, there is only a bulk sound velocity, thus there is no shear modulus or Poisson ratio.

Phase	P (GPa)	ρ (g/cm ³)	U_s (km/s)	u_p (km/s)	T (k)	C_b (km/s)	C_l (km/s)	G (GPa)	ν
hcp	88.4	2.696	12.340	3.872	1200	11.577	15.342	200.2	0.266
hcp	142	2.993	14.177	5.414	2540	12.736	16.142	220.8	0.302
hcp	179	3.171	15.240	6.349	3400	13.354	16.710	239.9	0.314
hcp	210.0	3.289	16.107	7.047	4400	13.842	16.811	224.5	0.341
bcc	136.4	2.993	13.895	5.306	2142	12.572	15.862	210.0	0.307
bcc	176.8	3.177	15.126	6.318	3262	13.280	16.302	213.0	0.331
bcc	203.9	3.289	15.872	6.944	4000	13.681	16.547	213.7	0.344
liquid	262.7	3.464	17.457	8.134	5068	14.736	***	***	***
liquid	323.0	3.650	18.816	9.279	6985	15.691	***	***	***
liquid	498.1	4.079	22.195	12.126	13530	17.344	***	***	***
liquid	797.8	4.60	26.862	16.056	27290	19.954	***	***	***

Table II: Direct-impact Hugoniot data for solid Be. v_f and U_s are the measured flyer plate and shock velocity, respectively. u_p , σ , and ρ are the inferred particle velocity, peak stress, and density, respectively.

Sample	v_f (km/s)	U_s (km/s)	u_p (km/s)	σ (GPa)	ρ (g/cm ³)
z1707N	7.46±0.05	12.46±0.23	4.02±0.04	92.6±1.3	2.73±0.03
z1707S	8.62±0.05	13.29±0.30	4.66±0.05	114.5±1.8	2.85±0.05
z1684N	9.36±0.05	13.78±0.17	5.07±0.05	129.1±1.3	2.93±0.03
z1684S	10.36±0.05	14.48±0.18	5.62±0.05	150.4±1.5	3.02±0.03
z1685N	10.94±0.05	14.76±0.19	5.95±0.04	162.6±1.6	3.10±0.04
z1685S	12.19±0.05	15.71±0.26	6.63±0.05	192.8±2.3	3.20±0.05

Table III: Sound velocity and shear stress measurements for Be. v_f and U_s are the measured flyer plate and shock velocity, respectively. u_p and σ are the particle velocity and peak stress,

respectively, determined from the DFT solid Hugoniot and the measured shock velocity. The longitudinal, C_l , and bulk, C_b , sound velocities were determined from wave overtake times. The Poisson ratio, ν , and shear modulus, G , were calculated from the sound velocities. The shear strength, $Y = 2\tau$ (τ is the shear stress), is the integrated area between C_l and C_b in the Lagrangian sound velocity vs. particle velocity plane. The six shots with $v_f > 10$ km/s melted, hence there is no longitudinal velocity, Poisson ratio, shear modulus, or shear strength.

Sample	v_f (km/s)	U_s (km/s)	u_p (km/s)	σ (GPa)	C_b (km/s)	C_l (km/s)	ν	G (GPa)	Y (GPa)
z1680N	7.49±0.08	13.86±0.17	5.16±0.06	132.2±3.4	12.98±0.30	16.50±0.54	0.30±0.04	229±24	3.41±0.40
z1680S	8.13±0.08	14.35±0.18	5.57±0.07	147.9±3.6	13.29±0.27	16.74±0.48	0.31±0.03	236±22	3.56±0.26
z1689N	8.32±0.08	14.62±0.24	5.80±0.10	156.9±4.1	13.40±0.30	16.36±0.49	0.34±0.03	203±21	2.70±0.19
z1688N	8.58±0.08	14.78±0.23	5.94±0.09	162.3±4.1	13.42±0.32	16.07±0.52	0.35±0.04	181±22	2.45±0.21
z1689S	9.16±0.08	15.29±0.23	6.37±0.10	180.2±4.3	13.99±0.30	15.46±0.46	0.42±0.03	103±16	1.22±0.17
z1688S	9.49±0.08	15.56±0.19	6.60±0.08	189.9±4.1	14.03±0.27	15.12±0.40	0.44±0.03	77±13	0.92±0.13
z1657N	9.61±0.08	15.65±0.28	6.67±0.12	193.2±4.8	14.09±0.36	14.66±0.43	0.47±0.03	40.2±9.1	0.47±0.10
z1681N	9.78±0.08	15.86±0.26	6.85±0.11	201.0±4.8	14.13±0.33	14.21±0.39	0.50±0.03	5.5±6.8	0.07±0.06
z1657S	10.76±0.08	16.77±0.27	7.55±0.12	234.4±5.4	14.18±0.33	***	***	***	***
z1708N	10.79±0.08	16.85±0.27	7.62±0.12	237.5±5.5	14.42±0.34	***	***	***	***
z1681S	10.97±0.08	17.04±0.27	7.78±0.12	245.3±5.5	14.40±0.32	***	***	***	***
z1624N	11.29±0.08	17.20±0.28	7.92±0.13	251.9±5.9	14.60±0.35	***	***	***	***
z1708S	12.00±0.08	17.80±0.31	8.42±0.15	277.4±6.4	14.66±0.38	***	***	***	***
z1624S	12.66±0.08	18.37±0.44	8.90±0.22	303±10	15.38±0.45	***	***	***	***

Figures

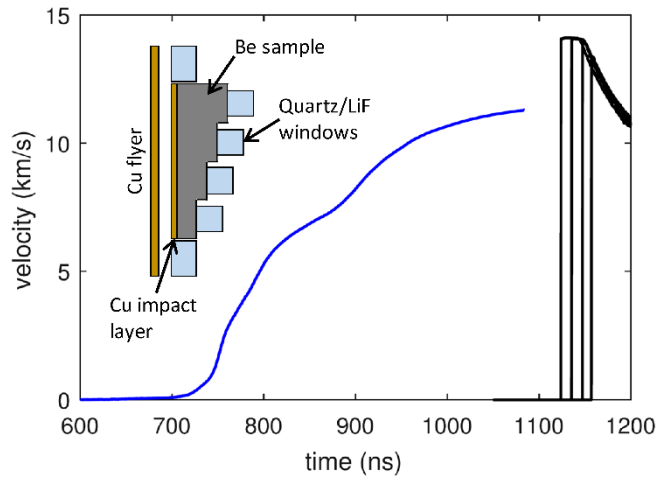


Figure 1: Representative VISAR data for an experiment with quartz windows (inset). The copper flyer plate velocity (blue line) was tracked from launch to impact with the windows adjacent to the stepped beryllium sample. Upon breakout of the shock from the Be sample into the quartz windows the shock velocity in the quartz is recorded at each step (black lines). The time between impact and shock breakout was used to determine the Be shock velocity.

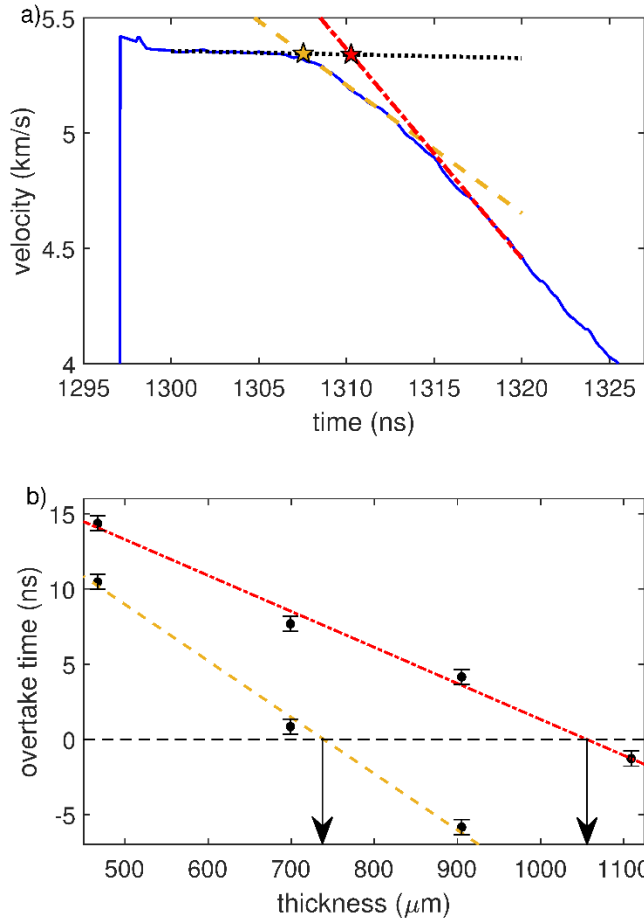


Figure 2: a) Typical overtake measurement in a LiF windowed experiment for solid Be. For stresses below melt, the Be release splits into a two-wave structure with the longitudinal wave propagating ahead of the bulk wave. The sudden drop in interface velocity upon rarefaction overtake indicated the overtake time for a given step. In samples where a two-wave structure is present, the intersection (stars) of linear fits to the constant plateau (dotted black line) and the longitudinal (dashed yellow line) and the bulk (dashed-dotted red line) releases is used to determine the overtake time. b) The thickness at which overtake would occur in an infinitely thick sample was determined by fitting the longitudinal and bulk overtake times as a function of the step thickness. The overtake thicknesses (arrows) are then determined by the $t_o = 0$ intercepts.

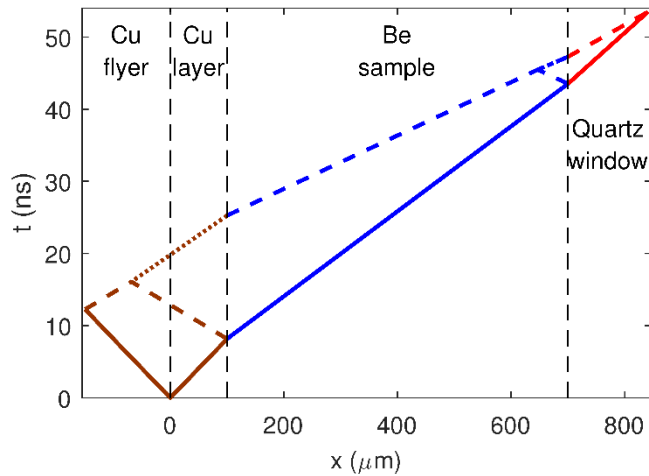


Figure 3: $x-t$ diagram of the rarefaction overtake in a thin Be sample. Upon impact of the Cu/Al flyer plate with the target, a shock (solid lines) is launched into the flyer plate and Cu layer on the target. When the shocks reach the Cu/Al interface (left axis) and Cu/Be interface, rarefaction waves (dashed lines) are launched into the flyer plate and Cu layer, respectively. These rarefaction waves interact, resulting in the overtaking rarefaction from the Cu/Al interface propagating through previously shocked and partially released copper (dotted line). Note that a similar wave interaction occurs near the Be/Quartz interface; in this case the overtaking rarefaction interacts with a recompression wave (quartz has a higher impedance than Be). However, the use of multiple thickness Be steps and extrapolation to $t_o = 0$, as shown in Fig. 2b, determines the overtake thickness in absence of these interactions (i.e. for an infinitely thick Be sample).

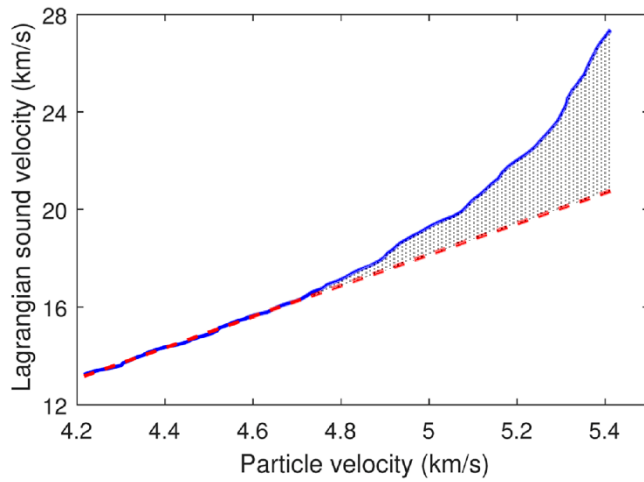


Figure 4: Representative shear stress calculation. The wave profile shown in Fig. 2a is used to determine the Lagrangian sound velocity as a function of the particle velocity (solid blue line). A linear fit (dashed red line) is used to estimate the bulk response up to the peak particle velocity. Integration of the area between the longitudinal and bulk curves gives an estimate of twice the shear stress.¹

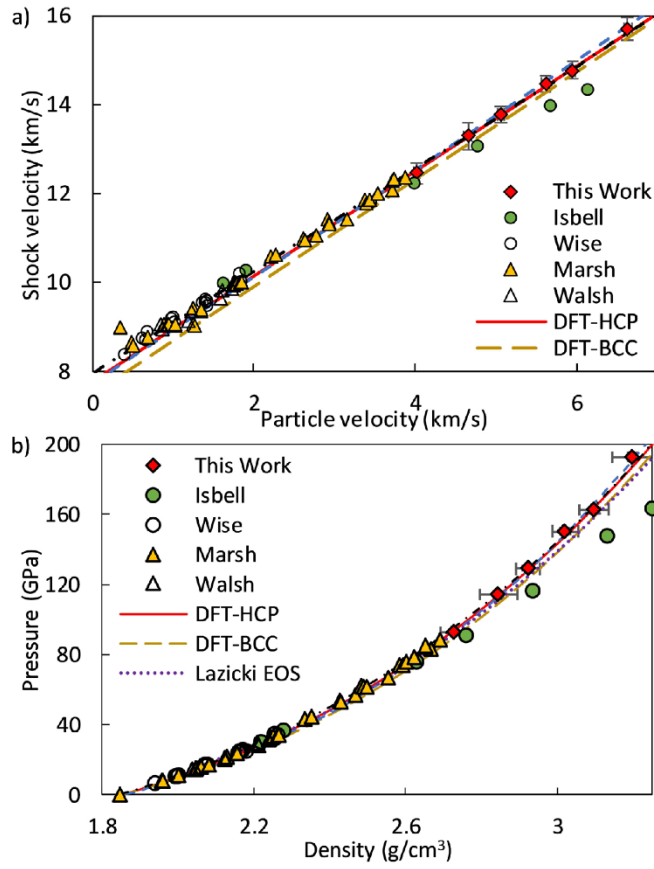


Figure 5: a) $U_s - u_p$ and b) $P - \rho$ Hugoniot for solid beryllium. This work (red diamonds) constrained the Hugoniot from 90-190 GPa, a range previously only measured by Isbell (green circles)²⁷. The current results are in good agreement with lower stress work by Wise (open circles)²⁶, Marsh (yellow triangles)²³ and Walsh (open triangles)²⁴ as well as the XEOS 40 (dashed blue line) and SESAME 2024 (dashed-dotted black line) tables. The Isbell data neither agree with the other legacy data nor the present results. The DFT Hugoniot fit for the hcp phase (solid red line) is in excellent agreement with the data (with the exception of the Isbell data that appears to be an outlier) over the entire region. In contrast, the DFT Hugoniot fit for the bcc phase (dashed orange line) is systematically more compressible, particularly at the lower stresses. The calculated Hugoniot using the Vinet EOS and Debye thermal expansion fits from

Lazicki (dotted purple line)²¹ is slightly more compressible than the present results. This discrepancy is likely due to the poor constraint for the thermal expansion fit noted by Lazicki.

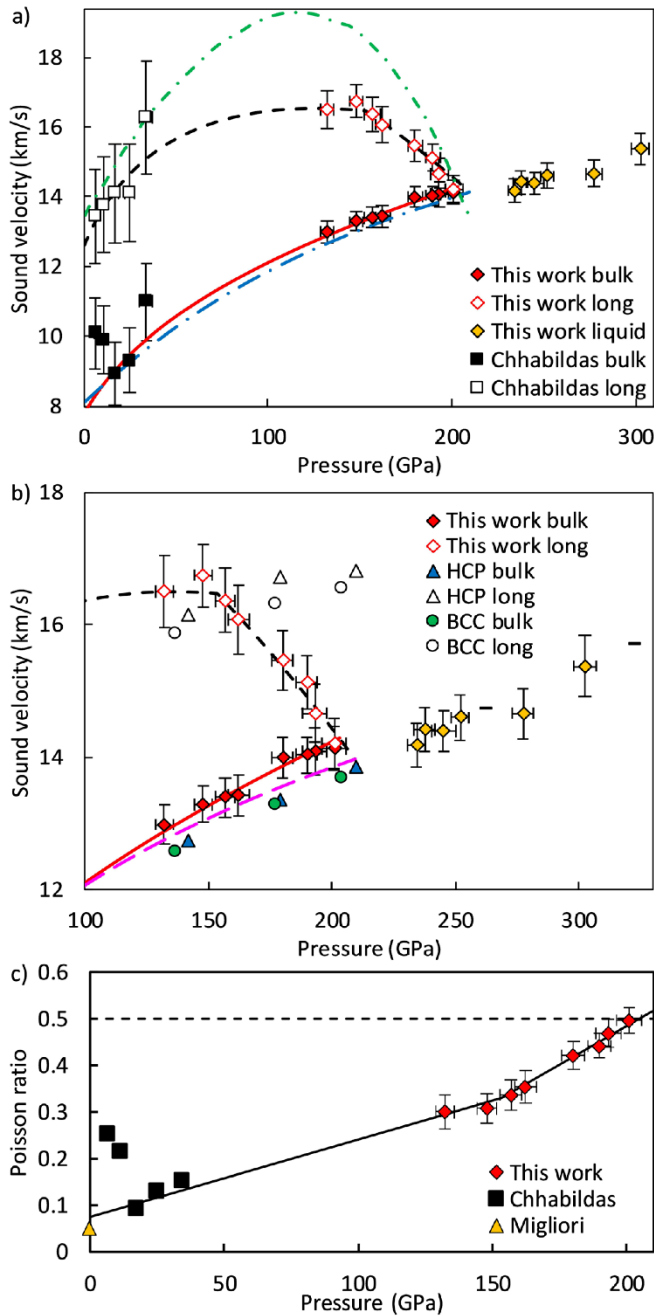


Figure 6: a) and b) Hugoniot sound velocity and c) Poisson ratio of beryllium. Below ~ 200 GPa, Be is solid as indicated by the existence of both longitudinal (open diamonds) and bulk (solid diamonds) release waves. The present results are in good agreement with earlier work by Chhabildas (squares)³². The bulk sound velocity (solid red line), determined from the DFT Hugoniot for the hcp phase and the ambient Grüneisen parameter, agrees with the experimental

data, as does the model by Ignatova⁵⁹ (dashed-dotted blue line). Calculation of the bulk velocity using the Grüneisen parameter determined from DFT calculations (long-dashed pink line) diverges from the ambient calculation above 130 GPa and is in better agreement with DFT calculations of the sound velocity (solid circles and triangles). The longitudinal velocity (dashed black line) was modeled using the bulk velocity (solid red line) and a piece-wise linear fit to the Poisson ratio (solid black line in (c)). Above 150 GPa, the longitudinal velocity exhibits a steady decrease, consistent with a softening of the shear modulus approaching melt. Prior to this decrease, the measured longitudinal velocities agree with DFT calculations for both the hcp (open triangles) and bcc (open circles) phases. In contrast to the bulk sound velocity, the longitudinal sound velocity from the model by Ignatova (dashed-dotted green line) is significantly higher than this work. The measured sound velocity in the liquid phase (yellow diamonds) is in good agreement with DFT calculations for liquid Be (dashes).

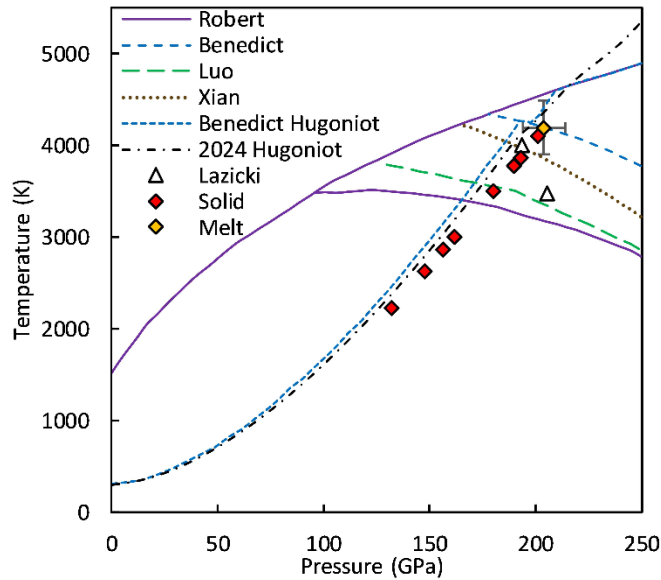


Figure 7: $P-T$ phase diagram of beryllium. Phase boundaries are from Robert (solid purple lines)¹⁵, Benedict (dashed blue line)¹⁴, Luo (long-dashed green line)¹⁶, and Xian (dotted brown line).¹⁷ We note that the Robert determined the melt boundary using a heat-until-melt method and thus should be viewed as an upper limit for the melt curve. Also shown are Hugoniot from the SESAME 2024 table (dashed-dotted black line) and Benedict (short-dashed blue line). The Hugoniot sound velocity experiments from this work that appear to have remained solid (red diamonds) do not provide conclusive evidence for the hcp-bcc transition. This is consistent with the highest $P-T$ results from Lazicki (open triangles)²¹ where they found Be to remain in the hcp phase. Taken together, these results are in reasonable agreement with the phase boundaries of Benedict and Xian, but disagree with the boundaries of Robert and Luo. However, as noted by Robert, the predicted location of the hcp-bcc boundary has large uncertainty due to the small enthalpy difference between the two phases. The experimentally determined onset of melt is shown as the yellow diamond. We stress that the temperature states for these experiments are not measured, but were determined from $T(P)$ obtained from the DFT hcp Hugoniot and ignore any

temperature increases due to dissipation; the actual temperature states may be higher than those shown here.

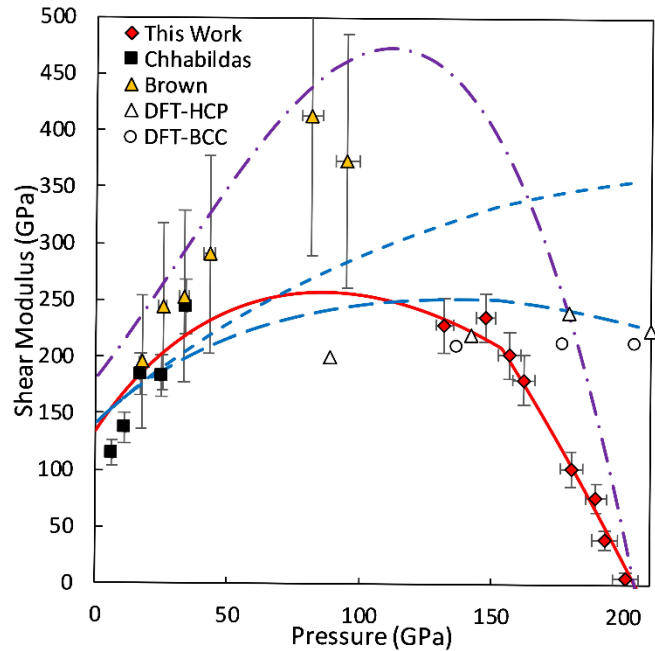


Figure 8: Pressure dependence of the shear modulus for Be. A fit to the Poisson ratio from this work and that of Chhabildas results in the shear modulus denoted by the red line. DFT calculations do not show a significant difference in the shear modulus of the hcp and bcc phases. Brown (yellow triangles)¹ reports a somewhat higher shear modulus from ramp compression experiments; this may be explained by the temperature difference between the Hugoniot and isentrope. The peak value of the shear modulus from this work is in reasonable agreement with DFT and results from the Burakovsky-Preston strength model (short-dashed blue line). In contrast, both the RING model (dashed-dotted purple line)⁶¹ and results from the Steinberg-Guinan model (long-dashed blue line) predict a shear modulus that is significantly larger than that inferred from this work.

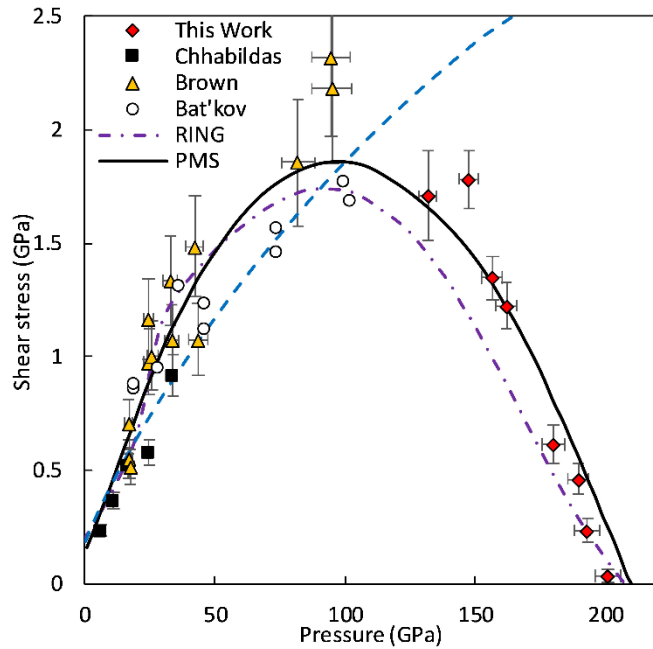


Figure 9: Pressure dependence of the shear stress (or half the shear strength) of Be. The shear stress in this work (red diamonds) is inferred from the offset between the bulk and longitudinal response of beryllium during release. These data are in good agreement with previous results by Chhabildas (black squares)³², Brown (yellow triangles)¹, and Bat'kov (open circles)⁶⁷. As an example of conventional non-relaxation models, the Steinberg-Guinan strength model (dashed blue line) agrees with data up to peak shear stress but fails to accurately represent the decrease in strength approaching melt. The PMS (solid black line)⁶⁸ and RING (dashed-dotted purple line)⁶¹ models developed by VNIIEF both accurately represent the data up to peak shear stress; however, the PMS model better represents the data approaching melt.